Voltage-dependent reconstruction of layered Bi_2WO_6 and Bi_2MoO_6 photocatalysts and its influence on charge separation for water splitting

Quinn Campbell,[*] Daniel Fisher, and Ismaila Dabo
Department of Materials Science and Engineering, Materials Research Institute, and Penn State Institutes of Energy and the Environment, The Pennsylvania State University, University Park, Pennsylvania 16802, USA

(Received 6 September 2018; revised manuscript received 6 December 2018; published 30 January 2019)

We study the surface stability of the layered bismuth-oxide Bi_2WO_6 and Bi_2MoO_6 photocatalysts, which belong to the series of Aurivillius ($Bi_2A_{n-1}B_nO_{3n+3}$) perovskites and have been proposed as efficient visible-light absorbers, due to favorable electronic hybridization induced by the bismuth 6s and 6p orbitals. We present a Newton-Raphson optimization of the charge distribution at the semiconductor-solution interface using the self-consistent continuum solvation (SCCS) model to describe the influence of the aqueous environment. Our analysis provides a description of the charged interface under controlled pH and applied voltage and offers a molecular interpretation of the competing structural and electrical factors that underlie the facet-dependent photocatalytic activity of layered $Bi_2A_{n-1}B_nO_{3n+3}$ compounds.

DOI: 10.1103/PhysRevMaterials.3.015404

I. INTRODUCTION

Artificial photosynthesis is uniquely positioned to alleviate the energy needs of the world population by converting water, carbon dioxide, and sunlight into fuels [1]. An outstanding challenge facing this technology is to develop photocatalysts of low cost and of high durability [2]. The search for new photocatalysts focuses on metal oxides due to their stability in water and their chemical versatility [3,4]. However, few of these oxides can absorb visible light, limiting their use as photoelectrodes. It is thus critical to optimize the band gap of these materials to enable them to operate efficiently under sunlight.

The fractional substitution of the cationic species that compose the metal oxides is an effective means to tune their band gap [5–8]. Nevertheless, this approach introduces compositional disorder that increases the rate of electron-hole recombination. In contrast, the intercalation of functional layers into metal oxides provides an effective method to control the band gap while preserving or enhancing charge separation [9]. An example of the effectiveness of this method to modify the electronic structure of WO_3 is shown in Fig. 1; the intercalation of bismuth oxide layer in WO_3 creates electronic states above the valence band maximum, thereby reducing the band gap of WO_3. In addition to WO_3, this method has been successfully used to enhance light absorption in a range of semiconducting ABO_3 and BO_3 metal oxides for use as photocatalytic electrode materials [10–17].

The ability to design metal oxides that are compatible with the solar spectrum by intercalating functional oxide layers provides a strong motivation to further study the photocatalytic activity of this family of layered semiconductors. In particular, the accurate determination of the photocatalytic mechanisms that take place on the surface of the electrode requires one to know the interfacial structure under applied voltage and controlled pH.

In this work, we address critical questions surrounding the surface termination of Bi_2WO_6 and Bi_2MoO_6, two prototypical layered oxides of the Aurivillius series, having the generic chemical formula $Bi_2A_{n-1}B_nO_{3n+3}$. Since different surface terminations exhibit different catalytic properties, knowing which terminations are most stable under varying environmental conditions is essential to narrowing down the choice of candidate photocatalysts and guiding their synthesis. Experimental studies by Saison *et al.* and Zhang *et al.* have shown that the (010) crystalline facet dominates the surface structure of Bi_2WO_6 and Bi_2MoO_6 particles in electrolytic media [20,21]. The (010) facet can exhibit multiple terminations, however, ending with either W/Mo tetrahedrons or Bi_2O_2 layers. While Zhang *et al.* have demonstrated that the stability of the (010) facet is strongly enhanced by the adsorption of oxygen species, the specific molecular arrangement of the oxygen-terminated surface is still poorly understood, precluding the analysis of photocatalytic trends as a function of surface structure.

First-principles modeling provides a powerful approach to investigating the surface stability and electrical response of solvated semiconductor electrodes with atomic-level precision and quantum-mechanical accuracy [22–25]. However, the application of this approach to layered photoelectrodes faces two major problems. The first is accessing the equilibrium charge-voltage response of their various surface terminations, and the second is assessing the surface free energy of different layers within the electrode.

Regarding the first problem, predicting the charge-voltage response of a semiconductor electrode entails describing the accumulation of charge at its surface and within the subsurface depletion region. Recently, we have developed a quantum-continuum model that incorporates an electronic-structure Kohn-Sham treatment of the surface region within a semiclassical Mott-Schottky representation of the depletion

---

[*] quinn.campbell@psu.edu

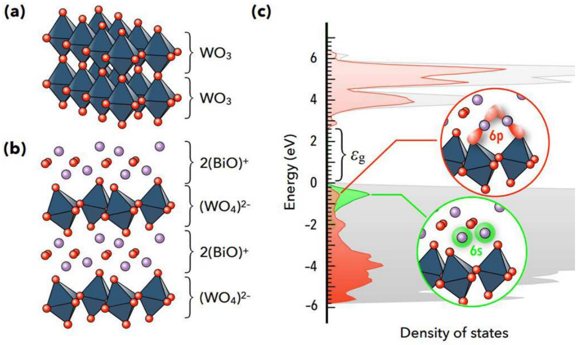

FIG. 1. The intercalation of bismuth oxide into the pseudocubic lattice of tungsten oxide WO_3 [panel (a)] generates a layered bismuth-oxide (Aurivillius) Bi_2WO_6 structure [panel (b)] that is characterized by strong hybridization of the bismuth 6s and 6p states with the valence bands of the original WO_3 oxygen 2p states as seen from the bismuth 6s (green) and 6p (red) projected density of states and from the total (gray) density of states including scissor corrections [18,19], dominated by the oxygen 2p orbital [panel (c)]. This hybridization causes the band gap ϵ_g of WO_3 to decrease, thereby enhancing its ability to absorb sunlight.

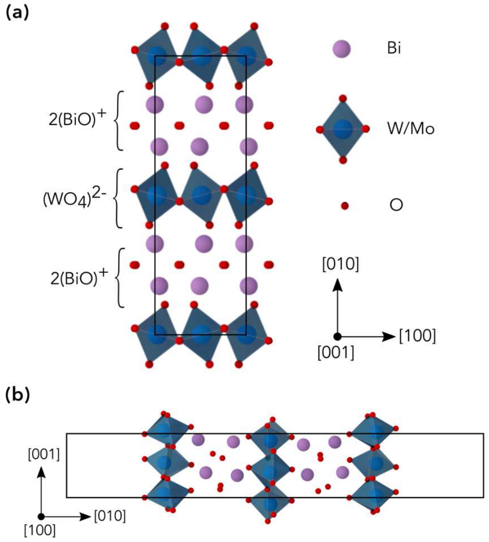

FIG. 2. (a) Layered structure of bulk Bi_2WO_6 and Bi_2MoO_6 compounds, showing the alternating tilt of the W and Mo octahedra upon geometry optimization. (b) Slab structure used for supercell surface calculations.

layer to provide a complete description of the electrification of the interface [26]. Nevertheless, the application of this quantum-continuum model requires the user to perform a number of self-consistent calculations to optimize the charge distribution between the surface and the bulk of the photoelectrode. Here, we circumvent this step by developing a robust, fully automated algorithm that directly converges to the optimal distribution. To solve the second problem, we extend previous methodologies to find the free energy of each ionic layer as a function of potential and pH, allowing us to consistently calculate the thermodynamic stability of the various terminations.

The paper is organized as follows. We present the electronic-structure computational procedure in Sec. II A and describe the finite-difference Newton-Raphson algorithm for simulating semiconductor electrodes under applied voltage in Sec. II B. We then generalize this approach in Sec. II C to predict the coverage-dependent surface free energy of layered semiconductors. Finally, Sec. III reports our computational results on the surface stability and junction characteristics of several Bi_2WO_6 and Bi_2MoO_6 terminations along the (100) and (010) orientations, with a focus on understanding the structural and electronic evolution of the surface during a potential sweep.

II. METHODS

A. Embedded electronic-structure calculations

To examine the structural properties of Bi_2WO_6 and Bi_2MoO_6, we first perform an optimization of their bulk crystalline geometry. We use the PW implementation of density-functional theory (DFT) within the QUANTUM-ESPRESSO distribution for materials simulation [27]. We employ the Perdew-Burke-Ernzerhof exchange-correlation functional [28] with pseudized atomic cores from the SSSP repository [29], which provides an extensively validated library of pseudopotentials. We use projector augmented wave-function (PAW) descriptions of the core orbitals. We sample the Brillioun zone with a shifted 4 × 2 × 1 Monkhorst-Pack grid and 0.03 Ry of Marzari-Vanderbilt smearing [30]. We select wave-function and charge density kinetic energy cutoffs of 150 Ry and 600 Ry, respectively. The resulting optimized bulk geometries are shown in Fig. 2(a). The calculated lattice parameters are $a = 5.56$ Å, $b = 16.84$ Å, $c = 5.59$ Å for Bi_2WO_6 and $a = 5.66$ Å, $b = 16.53$ Å, $c = 5.67$ Å for Bi_2MoO_6, in close agreement with experimental data [31].

To determine the voltage-dependent surface restructuring of Bi_2WO_6 and Bi_2MoO_6, we then create symmetric slab structures with the configuration shown in Fig. 2(b) and the surface terminations shown in Fig. 3. Specifically, for the (010) facet, we tested W/Mo terminated slabs with both one and two layers of Bi termination. For the (100) surface we just considered a unique termination, since the (100) crystalline orientation does not exhibit an alternating layer pattern. We center the slab in the supercell with a vacuum height of 14 Å. In all cases, a slab thickness of five layers is found to be sufficient to achieve a convergence of 50 meV for the Fermi energy and of 60 meV per unit cell for surface energies as shown in the Supplemental Material [32].

We employ the ENVIRON module, which implements a self-consistent continuum solvation (SCCS) model to describe the implicit immersion of the quantum system in aqueous media [33]. Dielectric cavities are introduced around each lateral facet of the slab with local dielectric permittivity written on the semiconductor side as $\epsilon(\boldsymbol{r}) = \exp[(\zeta(\boldsymbol{r}) - \sin(2\pi\zeta(\boldsymbol{r}))/2\pi)\ln\epsilon_{sc}]$ where ϵ_{sc} is the dielectric constant of the semiconductor; a similar expression can be taken for the solution with ϵ_{sc} replaced by the dielectric constant of the medium ϵ_m. Here, $\zeta(\boldsymbol{r}) = (\ln\rho_{max} - \ln\rho(\boldsymbol{r}))/(\ln\rho_{max} - \ln\rho_{min})$ is a

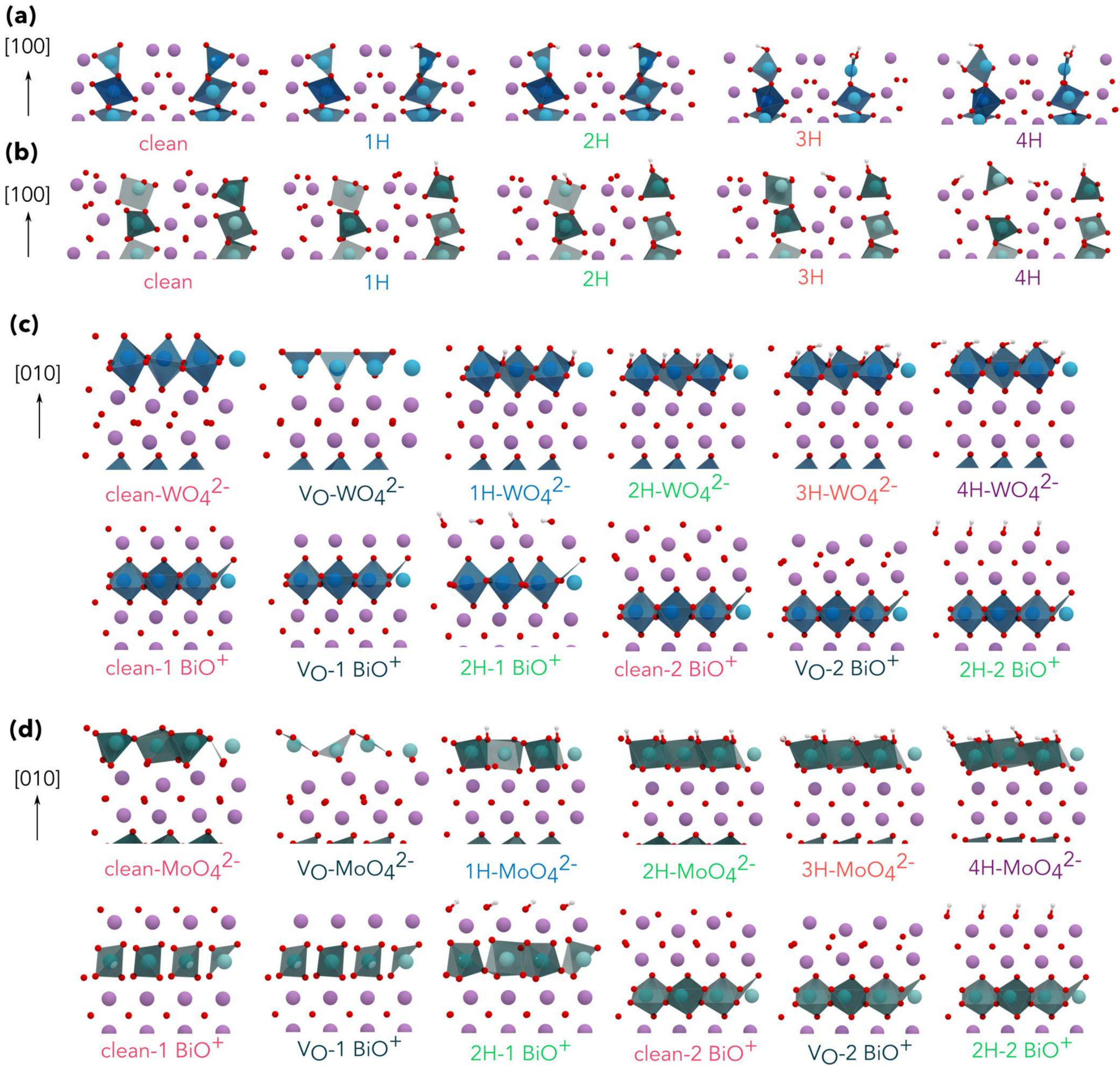

FIG. 3. Surface terminations for (a) Bi_2WO_6 (100), (b) Bi_2MoO_6 (100), (c) Bi_2WO_6 (010), and (d) Bi_2MoO_6 (010). The notation *n*H indicates *n* hydrogen adsorbed per unit cell. The (010) facet can be terminated with WO_4^{2-} layers, one or two BiO^+ layers. V_O indicates oxygen vacancies on the surface.

smooth switching function, marking the gradual dielectric transition between the quantum and continuum regions based on the charge density of the electrode, where ρ_{min} and ρ_{max} serve as the density thresholds specifying the inner and outer isocontours of the dielectric cavity. The SCCS model also includes contributions from the external pressure, solvent surface tension, and solvent dispersion and repulsion effects. The surface tension is described by $G_{\mathrm{cav}} = \gamma S$ and the dispersion and repulsion effects by $G_{\mathrm{dis+rep}} = \alpha S + \beta V$. Here, γ is the solvent surface tension, taken from experiment, α and β are fitted parameters, and S and V are the quantum surface and volume of the solute, defined as $S = \int d\mathbf{r}(d\Theta/d\rho)|\nabla\rho|$ and $V = \int d\mathbf{r}\Theta(\rho)$, where Θ is another smooth switching function, defined by $\Theta(\rho) = (\epsilon_{\mathrm{s}} - \epsilon(\rho))/(\epsilon_{\mathrm{s}} - 1)$. We use the parametrization of Andreussi *et al.*, where $\epsilon_{\mathrm{m}} = 78.3$ is the dielectric constant of the water, $\rho_{\mathrm{max}} = 5 \times 10^{-3}$ a.u., $\rho_{\mathrm{min}} = 1 \times 10^{-4}$ a.u., $\gamma = 72.0$ dyn/cm, and $\alpha = -22$ dyn/cm [33]. There has recently been some discussion that the introduction of the volume term is unphysical for slab surfaces, introducing an energy dependence on the overall size of the slab [34,35]. To clarify the impact of the volume parameter, we set $\beta = 0$ and compared final surface stability results. The elimination of the volume term led to minor changes in the final energy reported for each slab. Since the volume of all the slabs tested was roughly the same, however, the change in energy was essentially constant across all surfaces tested, leading to no alteration in the final reported surface stability. We use a dielectric constant for the semiconductor of $\epsilon_{\mathrm{sc}} = 5.7$, found from linear perturbation calculations [36].

B. Newton-Raphson charge optimization

In order to simulate the electrified semiconductor-solution interface, including the contributions from surface states to the charge-voltage response of the electrode, we employ the computational approach described in Ref. [26]. In this model, we embed a quantum-mechanical description in a semiconductor electrode surface between a Poisson-Boltzmann distribution of ionic charges and a Mott-Schottky distribution of charged defects on the electrolyte and semiconductor sides, respectively. We then impose that the Fermi energy be constant across the entire interface. To enforce this condition, we must determine the equilibrium amount of charge within the explicit surface region and the implicit bulk depletion region. For a detailed description of the computational procedure, we refer the reader to the Supplemental Material [32].

While our previously proposed computational approach solved the problem of aligning the Fermi level with the correct charge distribution manually, here we develop a numerical approach to iteratively optimize the charge on the explicit quantum-mechanical part of the system when the total charge on the electrode q is given. The charge q^{surf} is updated at each iteration n using the Newton-Raphson algorithm

$$q_{n+1}^{\mathrm{surf}} = q_n^{\mathrm{surf}} - (\Delta E_{\mathrm{F}})_n / (\Delta E_{\mathrm{F}})'_n, \tag{1}$$

where $(\Delta E_{\mathrm{F}})_n$ is the difference between the bulk and surface Fermi levels at iteration n, defined as

$$(\Delta E_{\mathrm{F}})_n = E_{\mathrm{F}}^{\mathrm{bulk}} - E_{\mathrm{F}}^{\mathrm{surf}}. \tag{2}$$

The derivative $(\Delta E_{\mathrm{F}})'_n$ with respect to the explicit charge of the quantum mechanical region is evaluated using the finite-difference equation

$$(\Delta E_{\mathrm{F}})'_n = ((\Delta E_{\mathrm{F}})_n - (\Delta E_{\mathrm{F}})_{n-1}) / \left(q_n^{\mathrm{surf}} - q_{n-1}^{\mathrm{surf}}\right). \tag{3}$$

Equation (1) leads to a smooth convergence of the charge starting from a reasonable estimate of the fraction of charge that is located in the explicit interface region. In specific terms for the Aurivillius compounds, we used $q^{\mathrm{surf}} = 0.7q$ as the initial condition with the frontier between the explicit and implicit of the semiconductor located two layers within the electrode and a dopant concentration of $10^{18}\ \mathrm{cm}^{-3}$ for both facets.

This method operates similarly to a structural optimization, involving a series of self-consistent field iterations. Convergence of surface charge within 1% of the total electrode charge typically requires ten Newton-Raphson steps. We developed this code within QUANTUM-ESPRESSO 6.1 and the ENVIRON 0.2 module [37].

C. Voltage- and pH-dependent stability

Calculating surface stability as a function of potential and pH also necessitates including (1) the chemical potential of the adsorbing species and (2) the chemical potential of the injected electronic charge in the evaluation of the surface energy. The free energy of a surface with N_{Bi} bismuth layers, N_{W} (N_{Mo}) tungsten (molybdenum) oxide layers, N_{H} hydrogen adsorbates, N_{O} oxygen adsorbates, and a charge q can be expressed as

$$\begin{aligned}\Delta G(N_{\mathrm{Bi}}, N_{\mathrm{W}}, N_{\mathrm{H}}, N_{\mathrm{O}}, q) \\ = \Delta G(N_{\mathrm{Bi}}, N_{\mathrm{W}}, N_{\mathrm{H}}, N_{\mathrm{O}}, q = 0) + \int_0^q \Phi(q')dq',\end{aligned} \tag{4}$$

where $\Phi(q)$ is the charge-dependent electrical potential of the interface. To calculate $\Delta G(N_{\mathrm{Bi}}, N_{\mathrm{W}}, N_{\mathrm{H}}, N_{\mathrm{O}}, q = 0)$ we evaluate the total energy of this structure, $E(N_{\mathrm{Bi}}, N_{\mathrm{W}}, N_{\mathrm{H}}, N_{\mathrm{O}}, q = 0)$, and subtract the chemical potential of each ionic species $\mu(\mathrm{BiO}^+)$ and $\mu(\mathrm{WO}_4^{2-})$, hydrogen ion $\mu(\mathrm{H}^+)$, and oxygen ion $\mu(\mathrm{O}^{2-})$:

$$\begin{aligned}\Delta G(N_{\mathrm{Bi}}, N_{\mathrm{W}} N_{\mathrm{H}}, N_{\mathrm{O}}, q = 0) \\ = E(N_{\mathrm{Bi}}, N_{\mathrm{W}}, N_{\mathrm{H}}, N_{\mathrm{O}}, q = 0) - N_{\mathrm{Bi}}(\mu(\mathrm{BiO}^+) - e_0\Phi) \\ - N_{\mathrm{W}}\left(\mu\left(\mathrm{WO}_4^{2-}\right) + 2e_0\Phi\right) - N_{\mathrm{H}}(\mu(\mathrm{H}^+) - e_0\Phi) \\ - N_{\mathrm{O}}(\mu(\mathrm{O}^{2-}) + 2e_0\Phi),\end{aligned} \tag{5}$$

where Φ is the electronic potential of the electrode, as previously proposed by Rong and coworkers for calculating surface free energy of oxide compounds [38,39].

Following the computational hydrogen-electrode method [40–42], the energy of hydrogen ions in solution can be determined from

$$\mathrm{H}^+ + e^- \leftrightarrow \tfrac{1}{2}\mathrm{H}_2(g), \tag{6}$$

which is at equilibrium at the potential of the reversible hydrogen electrode. Therefore the equilibrium chemical potential of H^+ is

$$\mu^\circ(\mathrm{H}^+) = \tfrac{1}{2}\mu^\circ(\mathrm{H}_2) + e_0\Phi^\circ_{\mathrm{H/H}^+}, \tag{7}$$

where $\mu^\circ(\mathrm{H}_2)$ is the energy of molecular hydrogen in the gas phase. We can then express the chemical potential of the solvated proton as

$$\mu(\mathrm{H}^+) = \mu^\circ(\mathrm{H}^+) - k_{\mathrm{B}}T\ln(10)\mathrm{pH}, \tag{8}$$

where k_{B} is the Boltzmann constant and $T = 300$ K is the ambient temperature. Similarly, the energy of removing an OH^- ion out of solution can be evaluated from

$$\mathrm{OH}^- + \mathrm{H}^+ \leftrightarrow \mathrm{H}_2\mathrm{O}, \tag{9}$$

yielding

$$\mu^\circ(\mathrm{OH}^-) = \mu^\circ(\mathrm{H}_2\mathrm{O}) - \mu^\circ(\mathrm{H}^+), \tag{10}$$

where $\mu^\circ(\mathrm{H}_2\mathrm{O})$ is approximated by the total energy of a single water molecule in vacuum. Noting that $\mathrm{pOH} = 14 - \mathrm{pH}$, we can find the chemical potential as

$$\mu(\mathrm{OH}^-) = \mu^\circ(\mathrm{OH}^-) - k_{\mathrm{B}}T\ln(10)(14 - \mathrm{pH}). \tag{11}$$

Finally, the energy of O^{2-} can be obtained from the equilibrium relation

$$\mu(\mathrm{O}^{2-}) = \mu(\mathrm{OH}^-) - \mu(\mathrm{H}^+). \tag{12}$$

With these equations in hand, we can determine the surface adsorbates as a function of potential and pH.

For calculating the terminal layer of the surface at equilibrium, we also need to determine the energy of removing

BiO^+ and WO_4^{2-} from the surface. To this end, we write the chemical reaction

$$\mathrm{BiO^+ + 2H^+ + 3}e^- \leftrightarrow \mathrm{Bi + H_2O}, \tag{13}$$

which is in equilibrium at $\Phi^\circ_{\mathrm{Bi/Bi^+}} = 0.320$ V (SHE) [43], and from which we can obtain the equilibrium chemical potential of BiO^+ in solution under standard conditions:

$$\mu^\circ(\mathrm{BiO^+}) = \mu^\circ(\mathrm{Bi}) + \mu^\circ(\mathrm{H_2O}) - 2\mu^\circ(\mathrm{H^+}) + 3e_0\Phi^\circ_{\mathrm{Bi/Bi^+}}, \tag{14}$$

where $\mu^\circ(\mathrm{Bi})$ is the energy of solid bismuth. We then express the chemical potential of the ideal solution as

$$\mu(\mathrm{BiO^+}) = \mu^\circ(\mathrm{BiO^+}) + k_\mathrm{B}T\ln[\mathrm{BiO^+}], \tag{15}$$

where $[\mathrm{BiO^+}]$ is the concentration of the BiO^+ ions. (For simplicity, we will consider an electrolyte saturated in BiO^+, eliminating the natural logarithm term.)

Similarly, we can calculate the energy of WO_4^{2-} with the following chemical reaction:

$$\mathrm{Ag_2WO_4} + 2e^- \leftrightarrow \mathrm{Ag + WO_4^{2-}}, \tag{16}$$

which is at equilibrium at $\Phi^\circ_{\mathrm{W/W^{2-}}} = 0.466$ V (SHE) [essentially the same chemical reaction can be used for MoO_4^{2-} at $\Phi^\circ_{\mathrm{Mo/Mo^{2-}}} = 0.4573$ V (SHE)] [43]. We can thus express the energy as

$$\mu^\circ\big(\mathrm{WO_4^{2-}}\big) = \mu^\circ(\mathrm{Ag_2WO_4}) - 2\mu^\circ(\mathrm{Ag}) - 2e_0\Phi^\circ_{\mathrm{W/W^{2-}}}, \tag{17}$$

where $\mu^\circ(\mathrm{Ag_2WO_4})$ is the energy of solid Ag_2WO_4, and $\mu^\circ(\mathrm{Ag})$ is the energy of solid silver. Finally, we derive the chemical potential as:

$$\mu\big(\mathrm{WO_4^{2-}}\big) = \mu^\circ\big(\mathrm{WO_4^{2-}}\big) + k_\mathrm{B}T\ln\big[\mathrm{WO_4^{2-}}\big], \tag{18}$$

where $[\mathrm{WO_4^{2-}}]$ is the concentration of the WO_4^{2-} ion in solution. We will again assume the solution is saturated with WO_4^{2-} ions.

With the energy of the solvated ions calculated, we can determine the equilibrium energy of each surface termination and adsorbate across a range of electrochemical conditions. These results are reported in the next section.

III. RESULTS AND DISCUSSION

We determine the electrochemical properties of Bi_2MoO_6 and Bi_2WO_6 by calculating the charge-voltage responses of their adsorbate-covered (100) and (010) facets, shown in Fig. 4. As explained previously, we consider terminations with $\mathrm{W/MoO_4^{2-}}$ layers and one or two layers of BiO^+. A first important observation is that the charge profiles of different adsorbates for all but the Bi_2WO_6 (100) surface are tightly clustered. This trend indicates that charge trapping by surface adsorbates plays a moderate role in the electrical response of Bi_2MoO_6 and Bi_2WO_6 and that the specific nature of the adsorbate does not strongly affect the distribution of charge across the interface.

To confirm and refine these observations, we calculate the Schottky barrier Φ_s of each termination. The Schottky barrier is the electronic barrier that develops between the

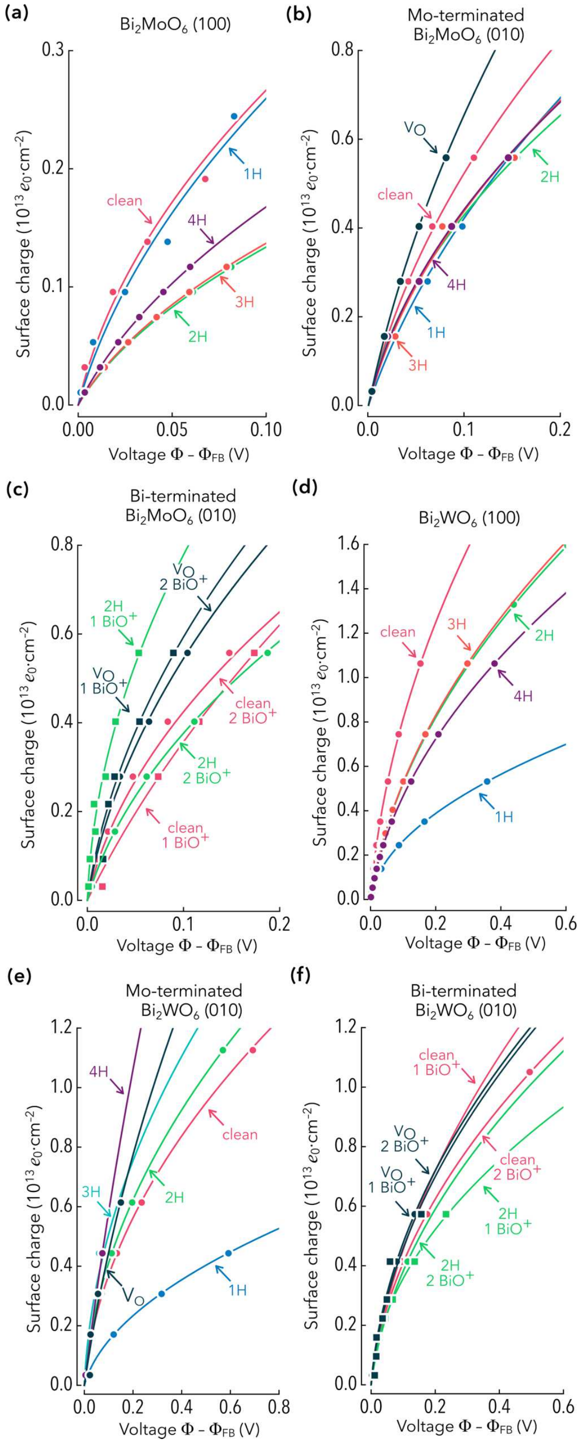

FIG. 4. Charge-voltage response of adsorbate covered Bi_2WO_6 and Bi_2MoO_6 photoelectrodes. (a) Bi_2MoO_6 (100), (b) Mo-terminated Bi_2MoO_6 (010), (c) Bi-terminated Bi_2MoO_6 (010), (d) Bi_2WO_6 (100), (e) W-terminated Bi_2WO_6 (010), and (f) Bi-terminated Bi_2WO_6 (010).

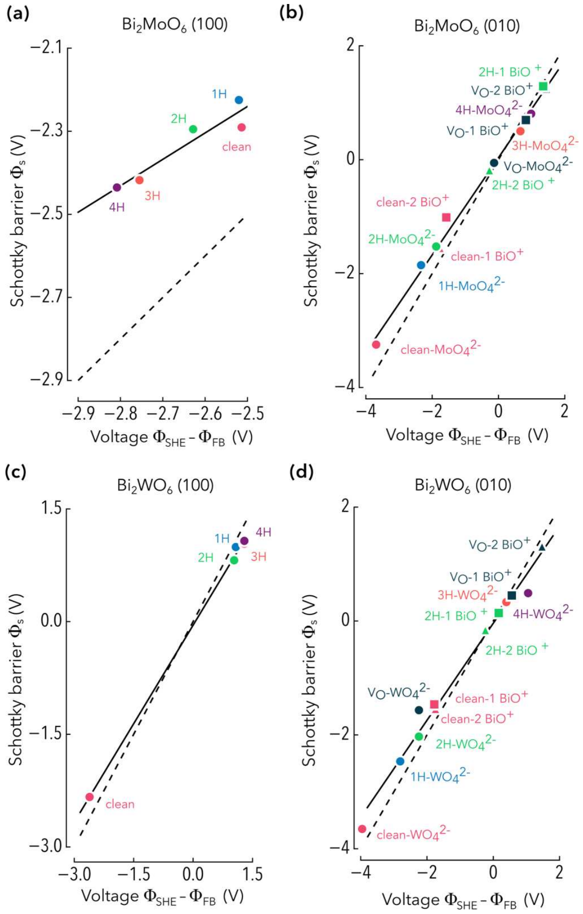

FIG. 5. Schottky barriers of different adsorbates and terminal layers at the (a) Bi_2MoO_6 (100), (b) Bi_2MoO_6 (010), (c) Bi_2WO_6 (100), (d) Bi_2WO_6 (010) surfaces. An ideal semiconductor junction would have a unit slope, $\mathscr{S} = 1$ (dashed line). The difference between the dashed line and the line of best fit shows the impact of surface states and adsorbates on lowering the Schottky barrier. The Bi_2MoO_6 (100), Bi_2MoO_6 (010), Bi_2WO_6 (100), Bi_2WO_6 (010) surfaces have slopes of $\mathscr{S} = 0.64$, 0.85, 0.87, and 0.85, respectively.

bulk of the semiconductor and the surface to compensate the difference between the donor and acceptor levels of the semiconductor and solution, respectively. It plays a decisive role in the ability of the interface to conduct photogenerated charge carriers from the bulk semiconductor to the surface and is thus a primary descriptor of the photocatalytic performance of a surface. In the limit of an ideal interface with no charge trapping induced by surface states, the Schottky barrier can be calculated as the difference between the electron-donating and electron-accepting levels on the semiconductor and solution side (Φ_{FB} and Φ), respectively. However, when adsorption or reconstruction induces surface states, the Schottky barrier height is renormalized by the charge-pinning fraction $\mathscr{S}$, yielding

$$\Phi_s = \mathscr{S}(\Phi - \Phi_{FB}). \tag{19}$$

Therefore, the charge-pinning fraction is a critical descriptor of the impact of surface states on the Schottky barrier [44–46]. To determine this important parameter, we calculate the Schottky barrier height of each surface as a function of the difference between the flatband potential and the standard hydrogen evolution potential, as shown in Fig. 5. These graphs show a linear trend with a slope of ∼0.85–0.87 for Bi_2WO_6 terminations and the Bi_2MoO_6 (010) termination. In contrast, the Bi_2MoO_6 (100) termination has a much lower charge pinning factor, ∼0.64. This reflects the wider variance in the charge-voltage curves of Bi_2MoO_6 (100) surface termination; the adsorption of hydrogen has strong repercussions on the surface dipole and charge distribution for this termination. It should be noted that we do not expect all of the terminations shown here to be stable at the large voltage range shown. These Schottky barriers should be taken as theoretical extrapolations for a metastable phase with a particular termination, allowing us to extract charge-pinning factors.

Having found the charge-voltage and Schottky barrier relationships, we turn our attention to determining the surface stability of each layer using the techniques outlined above. We calculate the surface stability as a function of potential at a pH of 7 as shown in Fig. 6. Both the Bi_2MoO_6 and Bi_2WO_6 (010) surfaces show a surface phase transition from one BiO^+ layer at negative potentials to surfaces terminated with two BiO^+ ions at higher potentials, with the Bi_2MoO_6 (010) surface seeing an additional phase transition to MoO_4^{2-} termination at voltages below –1.35 V. Notably, for both the Bi_2MoO_6 and the Bi_2WO_6 (010) surface, the unit cell with two BiO^+ terminating layers and two hydrogen adsorbed has nearly the same surface free energy as a pristine ("clean") surface terminated with only one BiO^+ layer, making it likely that a mixture between the two different terminations would form in solution. For the Bi_2MoO_6 (100) surface, the maximally hydrated surface termination tested was the most stable across a broad range of potential only giving way to a pristine interface at ∼0.9V. In contrast, for the Bi_2WO_6 (100) surface, the pristine surface is the most stable across a broad potential range, with hydrated surface terminations only becoming stable at lower voltages.

These electrochemical transitions are particularly important in light of the strong variation of the Schottky barrier height as a function of surface termination. In fact, for the Bi_2MoO_6 (010) surface, transitioning from a V_O-MoO_4^{2-} terminated surface to a V_O-1 BiO^+ and then to a 2H-2 BiO^+ surface leads to a change in Schottky barriers from –0.06 V to 0.70 V to –0.18 V. Since the Schottky barrier provides the motive force for charge separation and transfer of electrons from the bulk to the surface of the electrode, the highest magnitude Schottky barrier will see the highest efficiencies. This means the potential window where the V_O-1 BiO^+ surface dominates the Bi_2MoO_6 (010) termination will likely exhibit the most pronounced hydrogen generation. Similarly, the V_O-1 BiO^+ surface termination has the highest Schottky barrier of any stable structure for the Bi_2MoO_6 (010) surface with a Schottky barrier of 0.45 V. Notably, the high magnitude Schottky barrier of the Bi_2WO_6 (100) oxygen terminated surface is stable across a much broader range of potentials than for the Bi_2WO_6 (010) surface, providing a computational interpretation of the experimental conclusions

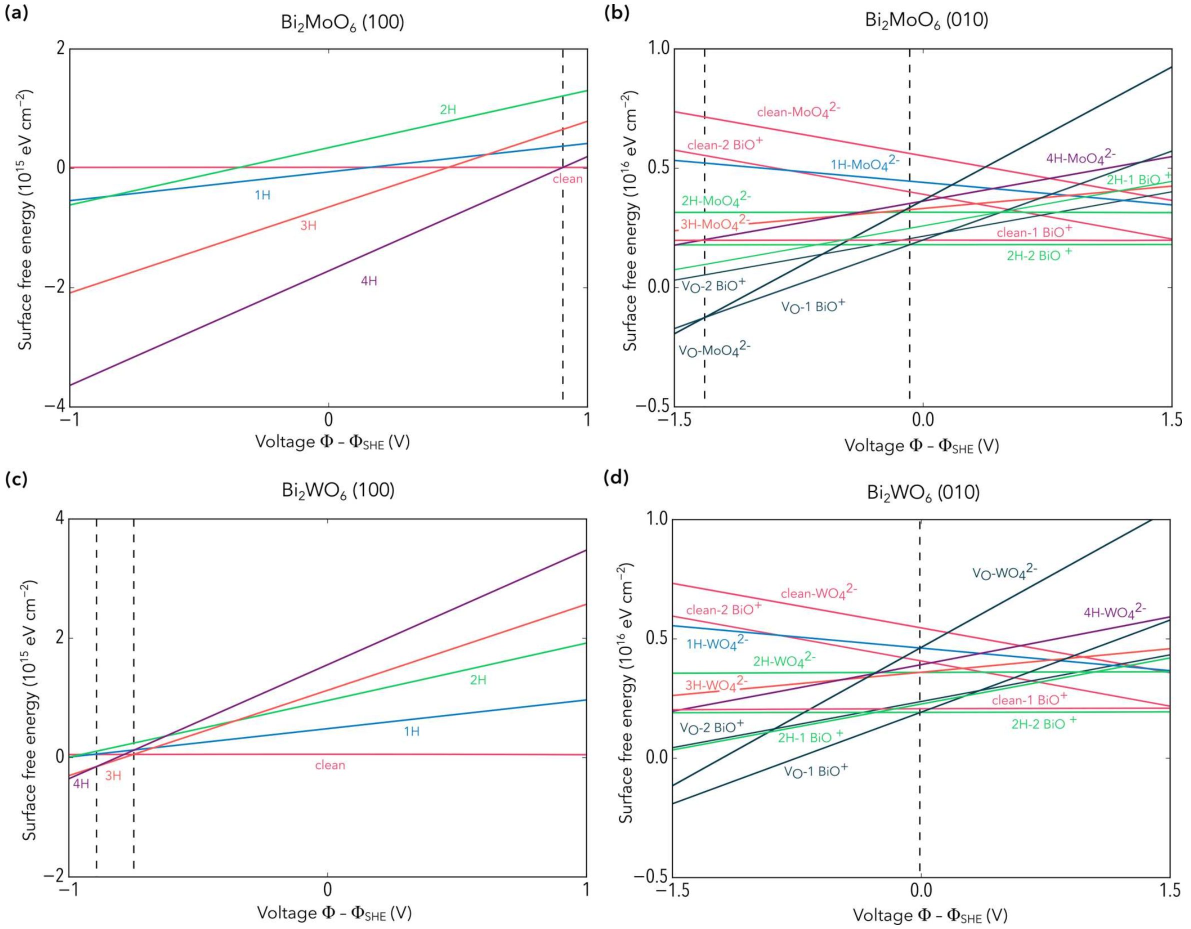

FIG. 6. Surface free energy of different adsorbates and layers at the (a) Bi_2MoO_6 (100), (b) Bi_2MoO_6 (010), (c) Bi_2WO_6 (100), (d) Bi_2WO_6 (010) surfaces, measured at pH = 7 under the assumption that the surrounding solution is saturated with BiO^+ and W/MoO_4^{2-} ions.

of Saison *et al.* [20] that the (100) facet is more active than its (010) counterpart.

IV. CONCLUSION

In summary, we calculated the surface structure and electrical characteristics of layered Aurivillius compounds from first principles, addressing the critical problems of determining the charge distribution between the semiconductor and its surface and of evaluating the surface energy of favored terminations. To calculate the equilibrium charge-voltage distribution of the semiconductor solution, we implemented a Newton-Raphson charge optimization algorithm that has enabled us to effectively compute the interfacial charge distribution as a function of the applied voltage. In addition, to obtain the surface-dependent termination and stability of each layer of the investigated materials, we calculated the energy of taking individual ionic layers out of solution as a function of potential and pH.

By combining these computational capabilities, we examined the Bi_2WO_6 and Bi_2MoO_6 (100) and (010) surfaces, showing a transition from a termination with a single bismuth layer to one with two bismuth layers. We further demonstrated that oxygen vacancies on a single-bismuth-layer termination gives the highest equilibrium Schottky barriers for both (010) surfaces. Finally, our analysis highlighted that the Bi_2WO_6 (100) surface has a more favorable Schottky barrier than the (010) surface over a wider potential range, providing electronic-structure evidence for the experimentally observed activity of the (100) surface. Computational studies such as the one presented here offer guidance in optimizing Aurivillius oxides for photocatalytic water splitting. In particular, our study suggests that the Bi_2WO_6 (100) facet should be a central target for the efficient separation of the photogenerated charge carriers.

ACKNOWLEDGMENTS

The authors acknowledge primary support from the National Science Foundation under Grant No. DMR-1654625 and partial support from the 3M Graduate Fellowship and Penn State University Graduate Fellowship.

[1] N. S. Lewis, MRS Bull. **32**, 808 (2007).

[2] J. R. McKone, N. S. Lewis, and H. B. Gray, Chem. Mater. **26**, 407 (2014).

[3] M. Woodhouse and B. A. Parkinson, Chem. Soc. Rev. **38**, 197 (2009).

[4] M. Woodhouse, G. S. Herman, and B. A. Parkinson, Chem. Mater. **17**, 4318 (2005).

[5] F. Wang, C. Di Valentin, and G. Pacchioni, J. Phys. Chem. C **116**, 8901 (2012).

[6] Y.-S. Hu, A. Kleiman-Shwarsctein, A. J. Forman, D. Hazen, J.-N. Park, and E. W. Mcfarland, Chem. Mater. **20**, 3803 (2008).

[7] Y. Ling, G. Wang, D. A. Wheeler, J. Z. Zhang, and Y. Li, Nano Lett. **11**, 2119 (2011).

[8] H. G. Kim, O. S. Becker, J. S. Jang, S. M. Ji, P. H. Borse, and J. S. Lee, J. Solid State Chem. **179**, 1214 (2006).

[9] A. Kubacka, M. Fernández-García, and G. Colón, Chem. Rev. **112**, 1555 (2012).

[10] H. G. Kim, D. W. Hwang, and J. S. Lee, J. Am. Chem. Soc. **126**, 8912 (2004).

[11] V. Thakral and S. Uma, Mater. Res. Bull. **45**, 1250 (2010).

[12] T. Saison, N. Chemin, C. Chanéac, O. Durupthy, L. Mariey, F. Maugé, V. Brezová, and J.-P. Jolivet, J. Phys. Chem. C **119**, 12967 (2015).

[13] F. Amano, K. Nogami, R. Abe, and B. Ohtani, J. Phys. Chem. C **112**, 9320 (2008).

[14] F. Amano, K. Nogami, and B. Ohtani, J. Phys. Chem. C **113**, 1536 (2009).

[15] Y. Shimodaira, H. Kato, H. Kobayashi, and A. Kudo, J. Phys. Chem. B **110**, 17790 (2006).

[16] C. Ng, A. Iwase, Y. H. Ng, and R. Amal, J. Phys. Chem. Lett. **3**, 913 (2012).

[17] L. Zhang, Y. Man, and Y. Zhu, ACS Catalysis **1**, 841 (2011).

[18] O. Gritsenko, R. van Leeuwen, E. van Lenthe, and E. J. Baerends, Phys. Rev. A **51**, 1944 (1995).

[19] M. Kuisma, J. Ojanen, J. Enkovaara, and T. T. Rantala, Phys. Rev. B **82**, 115106 (2010).

[20] T. Saison, N. Chemin, C. Chaneac, O. Durupthy, V. Ruaux, L. Mariey, F. Mauge, P. Beaunier, and J.-P. Jolivet, J. Phys. Chem. C **115**, 5657 (2011).

[21] L. Zhang, T. Xu, X. Zhao, and Y. Zhu, Appl. Catal., B **98**, 138 (2010).

[22] N. Kharche, J. T. Muckerman, and M. S. Hybertsen, Phys. Rev. Lett. **113**, 176802 (2014).

[23] T. A. Pham, Y. Ping, and G. Galli, Nat. Mater. **16**, 401 (2017).

[24] S. Selcuk and A. Selloni, Nat. Mater. **15**, 1107 (2016).

[25] L. Blumenthal, J. M. Kahk, R. Sundararaman, P. Tangney, and J. Lischner, RSC Adv. **7**, 43660 (2017).

[26] Q. Campbell and I. Dabo, Phys. Rev. B **95**, 205308 (2017).

[27] P. Giannozzi, S. Baroni, N. Bonini, M. Calandra, R. Car, C. Cavazzoni, D. Ceresoli, G. L. Chiarotti, M. Cococcioni, I. Dabo, A. Dal Corso, S. de Gironcoli, S. Fabris, G. Fratesi, R. Gebauer, U. Gerstmann, C. Gougoussis, A. Kokalj, M. Lazzeri, L. Martin-Samos, N. Marzari, F. Mauri, R. Mazzarello, S. Paolini, A. Pasquarello, L. Paulatto, C. Sbraccia, S. Scandolo, G. Sclauzero, A. P. Seitsonen, A. Smogunov, P. Umari, and R. M. Wentzcovitch, J. Phys.: Condens. Matter **21**, 395502 (2009).

[28] J. P. Perdew, K. Burke, and M. Ernzerhof, Phys. Rev. Lett. **77**, 3865 (1996).

[29] K. Lejaeghere, G. Bihlmayer, T. Björkman, P. Blaha, S. Blügel, V. Blum, D. Caliste, I. E. Castelli, S. J. Clark, A. Dal Corso, S. De Gironcoli, T. Deutsch, J. K. Dewhurst, I. Di Marco, C. Draxl, M. Dułak, O. Eriksson, J. A. Flores-Livas, K. F. Garrity, L. Genovese, P. Giannozzi, M. Giantomassi, S. Goedecker, X. Gonze, O. Grånäs, E. K. Gross, A. Gulans, F. Gygi, D. R. Hamann, P. J. Hasnip, N. A. Holzwarth, D. Iuşan, D. B. Jochym, F. Jollet, D. Jones, G. Kresse, K. Koepernik, E. Küçükbenli, Y. O. Kvashnin, I. L. Locht, S. Lubeck, M. Marsman, N. Marzari, U. Nitzsche, L. Nordström, T. Ozaki, L. Paulatto, C. J. Pickard, W. Poelmans, M. I. Probert, K. Refson, M. Richter, G. M. Rignanese, S. Saha, M. Scheffler, M. Schlipf, K. Schwarz, S. Sharma, F. Tavazza, P. Thunström, A. Tkatchenko, M. Torrent, D. Vanderbilt, M. J. Van Setten, V. Van Speybroeck, J. M. Wills, J. R. Yates, G. X. Zhang, and S. Cottenier, Science **351**, aad3000 (2016).

[30] N. Marzari, D. Vanderbilt, and M. C. Payne, Phys. Rev. Lett. **79**, 1337 (1997).

[31] V. K. Yanovskii and V. I. Voronkova, Phys. Status Solidi (a) **93**, 57 (1986).

[32] See Supplemental Material at http://link.aps.org/supplemental/10.1103/PhysRevMaterials.3.015404 for information on slab convergence and a detailed description of the semiconductor continuum method.

[33] O. Andreussi, I. Dabo, and N. Marzari, J. Chem. Phys. **136**, 064102 (2012).

[34] G. Fisicaro, L. Genovese, O. Andreussi, S. Mandal, N. N. Nair, N. Marzari, and S. Goedecker, J. Chem. Theory Comput. **13**, 3829 (2017).

[35] O. Andreussi and G. Fisicaro, Int. J. Quantum Chem. **119**, e25725 (2018).

[36] S. Baroni, S. De Gironcoli, A. Dal Corso, and P. Giannozzi, Rev. Mod. Phys. **73**, 515 (2001).

[37] Our implementation of a Newton-Raphson solver for the equilibrium charge-voltage behavior of a semiconductor can be found at https://github.com/quantumquinn/qe-environ-sc.

[38] X. Rong and A. M. Kolpak, J. Phys. Chem. Lett. **6**, 1785 (2015).

[39] X. Rong, J. Parolin, and A. M. Kolpak, ACS Catalysis **6**, 1153 (2016).

[40] I. C. Man, H.-Y. Su, F. Calle-Vallejo, H. A. Hansen, J. I. Martínez, N. G. Inoglu, J. Kitchin, T. F. Jaramillo, J. K. Nørskov, and J. Rossmeisl, ChemCatChem **3**, 1085 (2011).

[41] J. K. Norskov, J. Rossmeisl, A. Logadottir, L. Lindqvist, J. R. Kitchin, T. Bligaard, and H. Jonsson, J. Phys. Chem. B **108**, 17886 (2004).

[42] J. Rossmeisl, Z. W. Qu, H. Zhu, G. J. Kroes, and J. K. Nørskov, J. Electroanal. Chem. **607**, 83 (2007).

[43] A. J. Bard and R. Parsons, *Standard Potentials in Aqueous Solutions* (Marcel Dekker, New York, 1985).

[44] S. Kurtin, T. C. McGill, and C. A. Mead, Phys. Rev. Lett. **22**, 1433 (1969).

[45] L. J. Brillson, Phys. Rev. Lett. **40**, 260 (1978).

[46] A. J. Bard, A. B. Bocarsly, F. R. F. Fan, E. G. Walton, and M. S. Wrighton, J. Am. Chem. Soc. **102**, 3671 (1980).